ACS OMEGA

Open Access

http://pubs.acs.org/journal/acsodf

Article

Tuning Chemical and Morphological Properties of Ceria Nanopowders by Mechanochemistry

Maila Danielis,* Andrea Felli, Matteo Zampol, Nicolas Fonda, Philipp Brüner, Thomas Grehl, Erika Furlani, Stefano Maschio, Sara Colussi, and Alessandro Trovarelli*

Cite This: *ACS Omega* 2024, 9, 12046−12059

Read Online

ACCESS | Metrics & More | Article Recommendations | Supporting Information

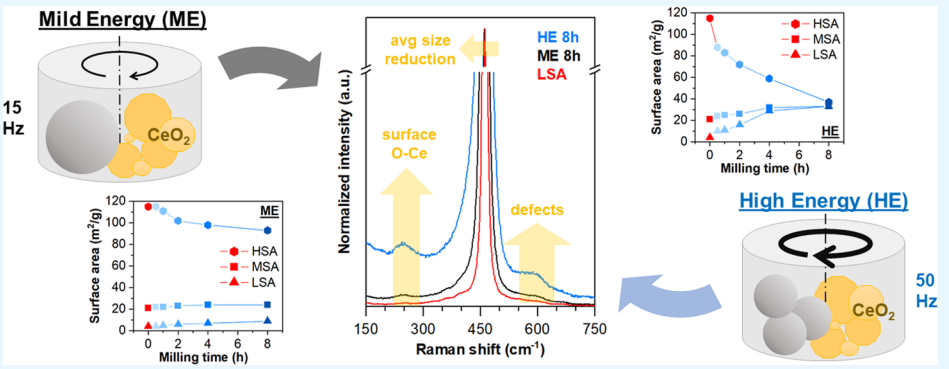

ABSTRACT: Cerium oxide powders are widely used and are of fundamental importance in catalytic pollution control and energy production due to the unique chemical properties of CeO_2. Processing steps involved in catalyst preparation, such as high-temperature calcination or mechanical milling processes, can alter the morphological and chemical properties of ceria, heavily affecting its final properties. Here, we focus on the tuning of CeO_2 nanopowder properties by mild- and high-energy milling processes, as the mechanochemical synthesis is gaining increasing attention as a green synthesis method for catalyst production. The textural and redox properties were analyzed by an array of techniques to follow the aggregation and comminution mechanisms induced by mechanical stresses, which are more prominent under high-energy conditions but strongly depend on the starting properties of the ceria powders. Simultaneously, the evolution of surface defects and chemical properties was followed by Raman spectroscopy and H_2 reduction tests, ultimately revealing a trade-off effect between structural and redox properties induced by the mechanochemical action. The mild-energy process appears to induce the largest enhancement in surface properties while maintaining bulk properties of the starting materials, hence confirming its effectiveness for its exploitation in catalysis.

INTRODUCTION

The control of ceria morphological properties, such as particle size and distribution, crystallinity, surface area, and pore size, is a matter of great interest for its application to electrodes and electrolytes, ceramic monoliths, and catalytic formulations.[1,2] Indeed, it has been extensively shown that the morphology of CeO_2 heavily influences its performance in many catalytic reactions,[3−5] improves its oxygen storage capacity,[6−9] increases thermal stability,[10−12] promotes the metal−support interaction of supported metals,[13−15] has a high ionic conductivity as electrolyte in solid oxide fuel cells,[16] and improves the mechanical and thermal stability of electrode layers.[17−19] In addition, recent advances in structured catalyst preparation have proposed 3D printing as a method to prepare cell-based monoliths composed entirely of the support oxide,[20−23] and it is well known that the size, shape, and distribution of starting powders is key to obtaining a printed manufact with solid mechanical resistance[24,25] as well as to improving flowability and processability in a scaled-up outlook.[26]

As a consequence, many different synthesis processes have been developed to increase control and tuning of these parameters, either on pure CeO_2 powders or in combination with dopant elements. The proposed methods often rely on solution-based routes,[10] high-temperature treatments,[27] hydrothermal steps for the preparation of cube- and rod-like nanostructures,[9] and, more recently, spray flame pyrolysis for uniform dispersion of CeO_2 crystallites.[28,29] The application of ball-milling has also been explored, yet mostly in relation with homogeneous distribution of CeO_2-based powders for subsequent ceramic sintering processes rather than catalytic

Received: December 12, 2023
Revised: January 25, 2024
Accepted: February 6, 2024
Published: February 27, 2024

applications,[30−33] but the environmental advantages allowed by a solvent-free milling method have been favoring its application.[34,35] In addition, the milling processes have also been demonstrated on a larger scale[36,37] compared to other preparation methods, such as hydrothermal or combustion based. The mechanochemical synthesis has indeed attracted increasing attention in the latest years for the synthesis of advanced nanomaterials, usually aimed at the preparation of alloys[38−40] or at materials phase-tuning[41,42] in high energy milling conditions. To the best of our knowledge, there have been no comprehensive approaches in the application of milling for tuning the surface chemical reactivity of a pure oxide.[43] Here, we underline the use of a simple mechanochemical approach as a tool for tuning the chemical properties of pure ceria for enhanced catalytic applications.

In the recent literature, the mechanochemical synthesis proved to lead to outstanding results in metal-supported heterogeneous catalysts,[44−47] for example generating unique interactions at the ceria surface when comilled with palladium (as Pd acetate or metallic Pd black)[44,48−50] in the absence of other solvents, and inducing peculiar configurations in bimetallic catalysts.[47,51] Remarkably, these interactions, and the correlated unusual morphology observed by HRTEM,[44,50] are only generated by mild-energy milling processes,[52] in contrast with the milling conditions generally reported for the preparation of advanced nanomaterials via ball-milling.[46,53] Scalability of the mild-energy milling process was also demonstrated in the 10−20 g scale in a planetary ball mill system.[54] However, the use of mild-intensity milling conditions, such as a low number of milling spheres or revolution per minutes (RPMs), is largely unexplored in the literature, as the low- and mild-intensity ranges are considered less effective in inducing variations in the processed powders compared to the high-energy counterpart.[33,55−57] Consequently, a systematic study of the effect of mild-energy conditions on the morphology and chemistry of the support oxide powders is still missing. In previous works carried out by our group[49,50] and others,[45,55] the milling parameters were optimized aiming at promoting the interaction between the metal of choice and the support oxide and the ceria particles were subsequently affected. Here, we show the effect of milling on the most important morphological properties of CeO_2 for catalytic applications and processing, measured by surface area and pore size analysis, X-ray diffraction (XRD), particle size distribution by laser diffraction, and SEM images. Additionally, their surface and redox properties were explored by Raman spectroscopy and H_2-TPR, with CO oxidation used as the probe reaction, highlighting the potential of the dry milling route for the appropriate tuning of the support oxide morphology and surface chemical properties depending on the starting CeO_2 materials.

RESULTS AND DISCUSSION

Morphological Features. Morphological and textural properties of the prepared CeO_2 powders before milling are summarized in Table 1. Calcination at different temperatures (550, 900, 950, and 1200 °C) was carried out to achieve a range of materials with different surface area, average crystallite size, and redox properties.

Starting from each material, the morphology and chemistry were investigated as a function of milling time and energy, following the evolution of CeO_2 micro- and mesostructure after exposure to mechanical energy. In Figure 1, the effect of medium-energy (ME) and high-energy (HE) milling conditions on the measured BET surface area of ceria powders is reported, clearly highlighting how the mild energy process has a negligible effect on the surface area of the CeO_2 powders, especially within 1 h of milling time, while gradual changes are observed at longer milling times. Conversely, under HE conditions (Figure 1b), similar trends can be observed but with appreciably faster variations compared to ME. The full list of values is reported in Table S1. Depending on the initial surface area values, an increasing or decreasing trend is observed, in agreement with the expected aggregation−disaggregation mechanisms occurring during dry milling of ceramic powders[33,58,59] where the starting powder size plays a crucial role. Remarkably, under HE operation, after 8 h, the same surface area is achieved on all samples, suggesting that an equilibrium condition is achieved between aggregation and breaking mechanisms. To prove this, a CeO_2-ESA (equilibrium surface area) sample was obtained by calcining CeO_2 powders at 900 °C for 4 h (see Table 1) and was subsequently milled at HE, showing stationary properties in terms of surface area (Figure S1).

Table 1. Summary of Textural Properties of the Starting CeO_2 Powders

sample	short name	calcination temperature (°C)	BET surface area (m^2/g)	BHJ pore volume (cm^3/g)	average CeO_2 crystallite size[a] (nm)
CeO_2—high surface area	HSA	550	115	0.34	9
CeO_2—medium surface area	MSA	950	21	0.19	41
CeO_2—low surface area	LSA	1200	4	0.10	71
CeO_2—equilibrium surface area	ESA	900	35	0.32	28

[a]Calculated by Scherrer's equation.

For catalytic purposes, the total surface exposed by the solid materials to gaseous reactants is a key parameter. However, its value is affected by several textural properties of the powder catalyst, including the crystallite dimension, particle size, and internal porosity. The latter was analyzed by the desorption branch of the N_2 physisorption isotherms, revealing that the intra- and interparticle porosities are also affected by the milling process. Figure 2 reports the pore size distribution profiles of all samples as a function of increasing milling times. The fresh CeO_2 powders (red lines) show distinct porosity, with a larger average pore size and a smaller total volume with increasing calcination temperature, as expected by the sintering effect of thermal treatments. After milling, on all investigated samples, a progressive reduction in the total pore volume was detected (Figure S2) while the pore size distribution varied depending on milling energy and starting material: under mild-energy conditions, MSA and LSA samples retained the initial pore structure while the initial pores around 8 nm of the HSA catalyst were slowly reduced into the 3−4 nm range (Figure 2a). Remarkably, high-energy milling yielded a similar pore distribution on all samples, regardless of the initial porosity. These 3−4 nm pores also appear on the ESA sample (Figure S3), where the total surface area was measured to be constant throughout the milling process, revealing that the net zero

https://doi.org/10.1021/acsomega.3c09926
ACS Omega 2024, 9, 12046−12059

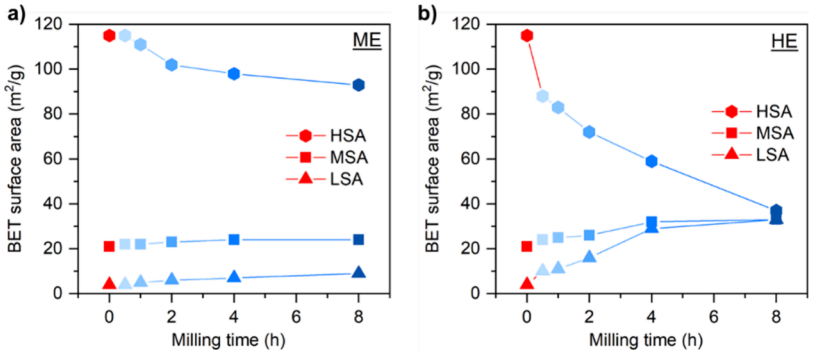

Figure 1. Evolution of surface area of CeO_2 powders at increasing milling times under (a) mild (ME) and (b) high (HE) milling energies.

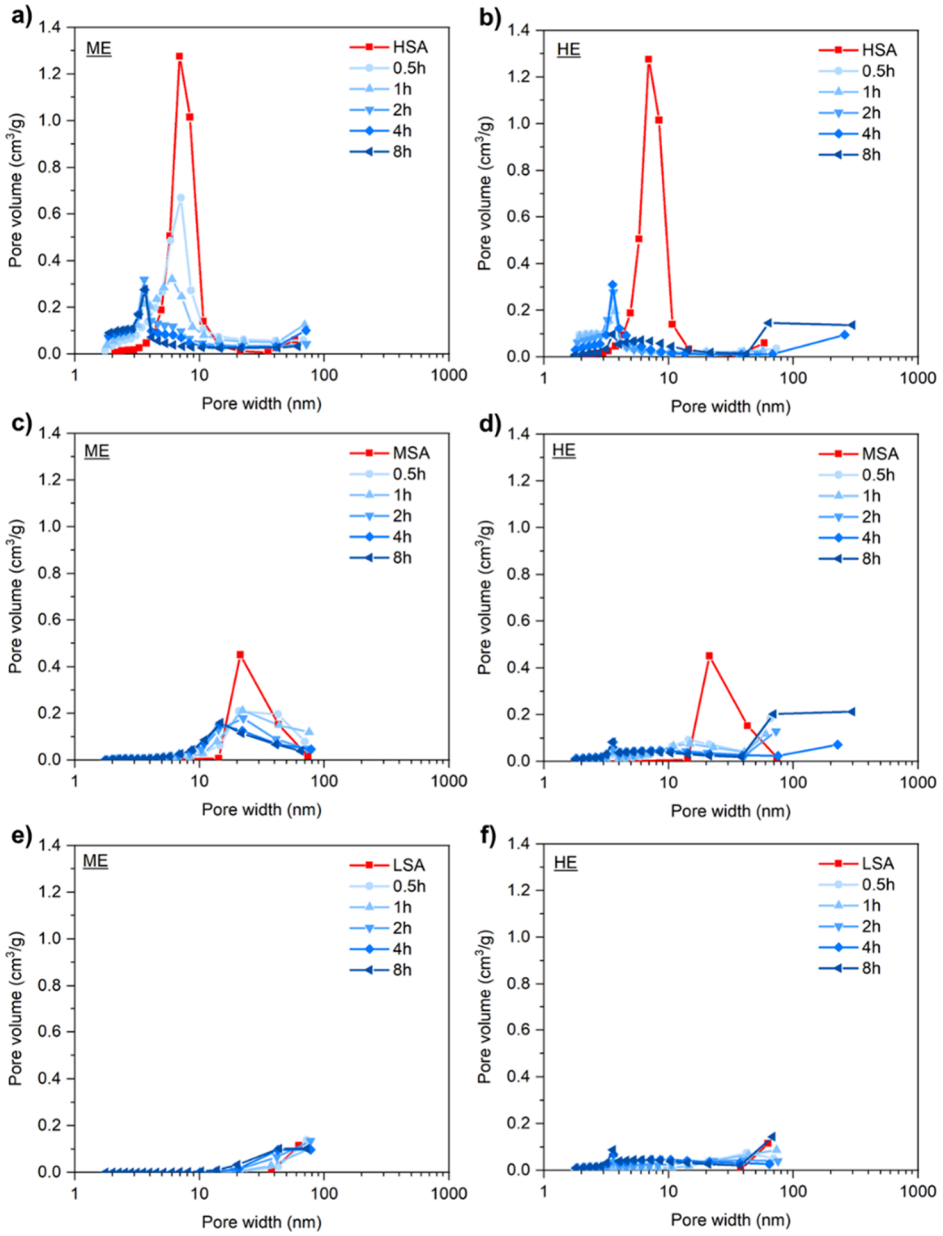

Figure 2. Pore size distribution measured on (a, b) HSA sample, (c, d) MSA sample, and (e, f) LSA sample after milling at mild-energy (ME) and high-energy (HE) conditions and at increasing milling times.

change in surface area is ultimately due to a balance in all textural changes induced by milling.

In addition to the total surface area of the ceria powders, the crystalline state of the CeO_2 fluorite lattice is also affected, as shown in Figures S4 and S5 by the full X-ray diffractograms. In

https://doi.org/10.1021/acsomega.3c09926
ACS Omega 2024, 9, 12046−12059

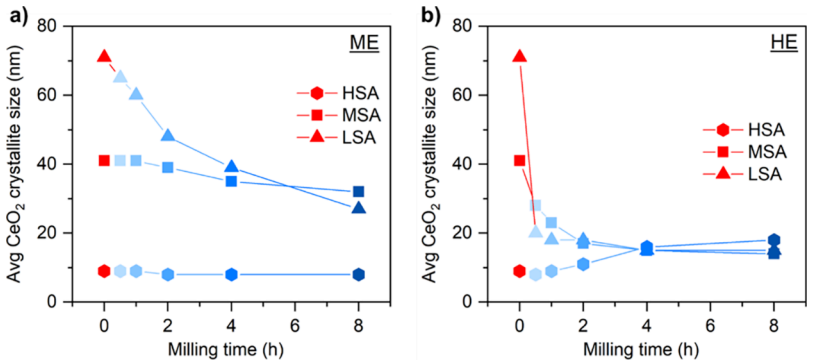

Figure 3. Evolution of average crystallite size estimated via Scherrer's equation of CeO_2 powders at increasing milling times under (a) mild (ME) and (b) high (HE) milling energies.

Figure 3, the evolution of the average crystallite size estimated using the Scherrer's equation on the CeO_2(111) main peak at 28° are summarized and reported as a function of milling time and intensity. Contrarily to surface area measurements, the milling process mainly yields a reduction in crystallite size, which is particularly significant on the samples calcined at higher temperatures (ESA, MSA, and LSA). The only exception is represented by the CeO_2-HSA-HE powders, where fusion of small grains into larger crystallites can be observed. Likely, the balance between crystallite size reduction and decreased porosity contributes to the measured evolution of the total surface area, as reported in Figure 1. In addition to the average grain size, the energy released through impacts and stresses during milling also results in a strained lattice, as clearly highlighted by the widening of the CeO_2 lattice peaks in the full diffractograms (Figure S4) and in the fitting values obtained by Rietveld refinement (Table S2). Since high strain can partially alter the estimation by Scherrer's formula, for comparison purposes, particle size values obtained by the Rietveld refinement and Williamson−Hall methods are reported in Table S3 for reference samples.

To exclude an effect of Zr doping from the milling media leading to high surface area, high strain, and small crystallite size, the XRD patterns were analyzed by the Rietveld method and no shifting in cell parameter coherent with bulk Zr doping was detected (Table S2).[60,61] ICP-MS analyses were carried out on the samples subjected to the harshest milling conditions, resulting in a negligible amount of Zr present on the catalyst (Table 2), confirming that the measured strain is predominantly induced by the mechanochemical stresses generated during the dry milling process.[58] However, the small amount of Zr detected by ICP analysis might be localized only over the CeO_2 surface, possibly leading to enhanced surface properties. Thus, LEIS analysis was performed and the results reported in Table S4 confirm that a very small amount of Zr is present on the surface of the milled CeO_2 powders. The maximum coverage, equal to 0.8% on the LSA-HE-8h sample, is in line with ICP data and suggests that the inclusion of Zr is uniform throughout the sample. On the other hand, mild-energy milled samples show very little Zr values, lower than the LEIS detection limit (0.2%), corroborating the expected correlation between milling intensity and contamination from the milling media.

Table 2. ICP-MS Quantitative Analysis of Zr Content in CeO_2 Powders after the Longest Exposure (8 h) to HE Milling Conditions

sample	Zr (wt %)	Zr/(Ce+Zr)[a] (%)
HSA-HE-8h	0.12	0.23
MSA-HE-8h	0.53	0.99
LSA-HE-8h	0.61	1.14

[a]Calculated as the atomic ratio between Zr and total Zr+Ce cations.

In addition to the size and crystallinity of grains,[62,63] milling processes are known to influence the average particle size, intended as the average dimension of the crystallite aggregates.[33,38,64] This parameter is fundamental for the processability of the powders, where a uniform distribution is usually required for the best performances.[24,26] By dynamic laser scattering, the particle size distribution of the CeO_2 samples before and after milling was investigated, showing uniform distribution after calcination ($d_{50} \approx 8$ mm) and a gradual multimodal profile following the mechanical action of the milling process. The cumulative curves are reported in Figure S6, while Figure 4 illustrates the histograms for each class size (below 2 mm, between 2 and 15 mm, and above 15 mm). By analyzing the growth of the smallest and largest class sizes, compared to the calcined samples that have >90% particles in the central fraction, we can follow the comminution and coalescence mechanisms on the particle aggregates. Compared to surface area and crystallite size trends, PSD profiles show a less linear trend, likely due to the competing nature of the two mechanisms.[59,64] However, it clearly appears that HE milling conditions promote agglomeration of the particles, with a significant shift of the particle size distribution toward larger sizes (>15 mm) (Figure 4b,d,f). Conversely, the effect of the ME milling process depends more strongly on the starting material, promoting agglomeration on the small HSA powders (Figure 4a) and favoring disaggregation on the larger MSA and, most noticeably, LSA samples (Figure 4c,e, respectively). These effects can also be appreciated when looking at the evolution of the d_{50} and d_{80} on all samples as a function of milling time and energy, shown in Figure 4g,h and Figure S7 for the ME and HE conditions, respectively. The odd behavior exhibited by the samples with low and medium initial surface area suggests that, on these catalysts, the ME process likely affects the surface properties to a larger extent compared to bulk features, thus escaping macroscopic morphological and textural analyses and leading to weaker interparticle forces and/or looser agglomerates, which are more easily disaggregated during sonication before PSD measurements.

https://doi.org/10.1021/acsomega.3c09926
ACS Omega 2024, 9, 12046−12059

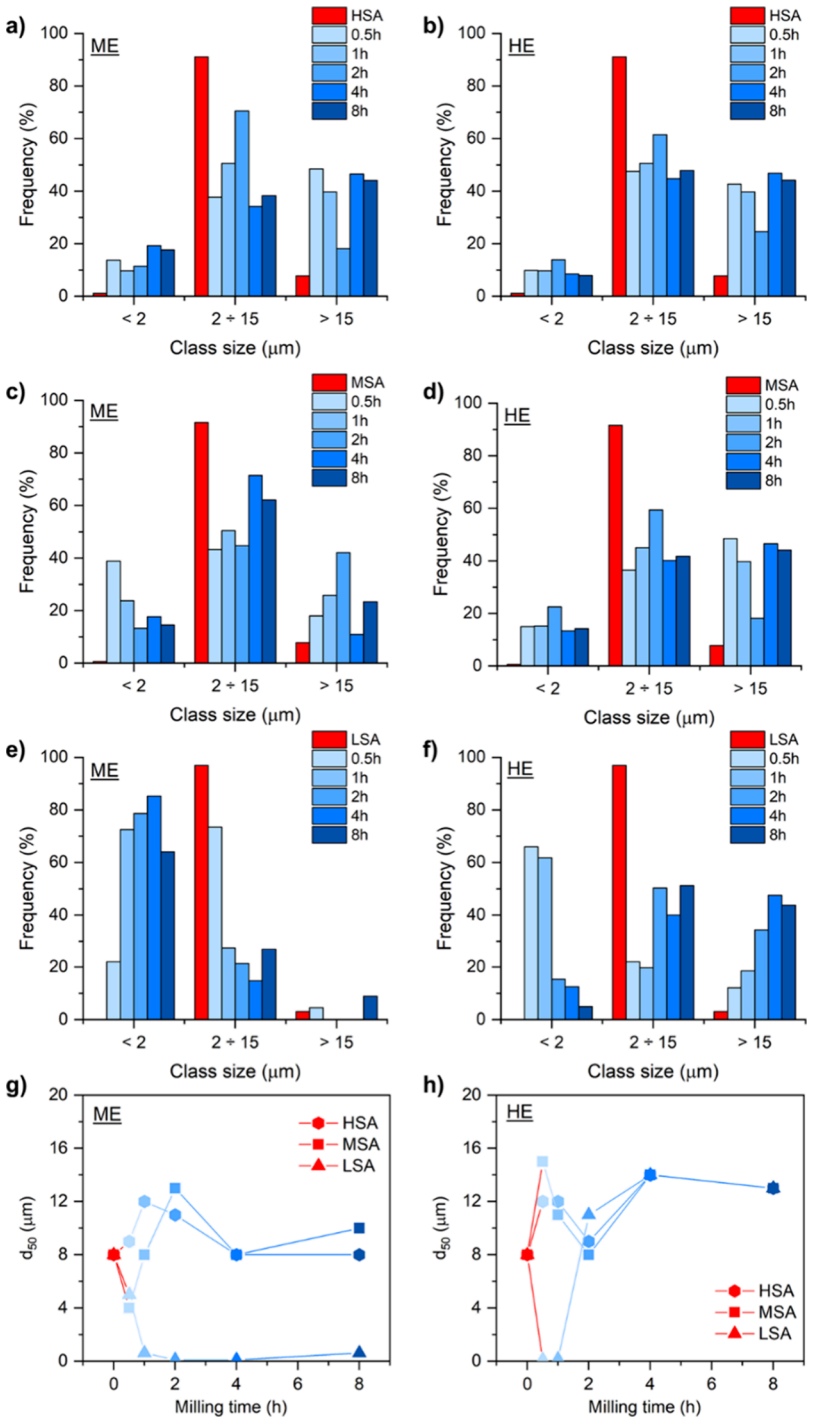

Figure 4. Distribution of CeO_2 particle size at increasing milling times; (a, b) HSA sample, (c, d) MSA sample, and (e, f) LSA sample. Evolution of the d_{50} on all samples as a function of milling time and energy: (g) mild energy (ME), (h) high energy (HE).

The inhomogeneous dispersion of particle aggregates on the samples induced by milling is well observed by SEM images (Figure 5), where representative images of the samples with the same surface area (*ca.* 30 m^2/g), namely, CeO_2-ESA, and the HSA, MSA, and LSA samples milled at HE for 8 h, are reported. In line with PSD curves, the calcined-only ESA sample exhibits uniform distribution of CeO_2 particles (Figure 5A−C), while on the milled samples, the presence of both smaller and larger agglomerates can be detected, irrespective of the starting CeO_2 powders properties (HSA: Figure 5D−F, MSA: Figure 5G−I, LSA: Figure 5J−L).

Surface Chemistry and Redox Properties. The morphological and textural properties of CeO_2 powders were shown to be affected to varying degrees by the ME or HE impacts generated during the milling process. All these factors contribute to tuning the chemical behavior of ceria. Moreover, mechanochemical changes and activation on powders are known to proceed from the surface inward,[56,65] and thus, it can be expected to lead to a large number of defects on the CeO_2 surface, the latter representing the active phase for heterogeneous catalytic reactions in the gas phase.

https://doi.org/10.1021/acsomega.3c09926
ACS Omega 2024, 9, 12046−12059

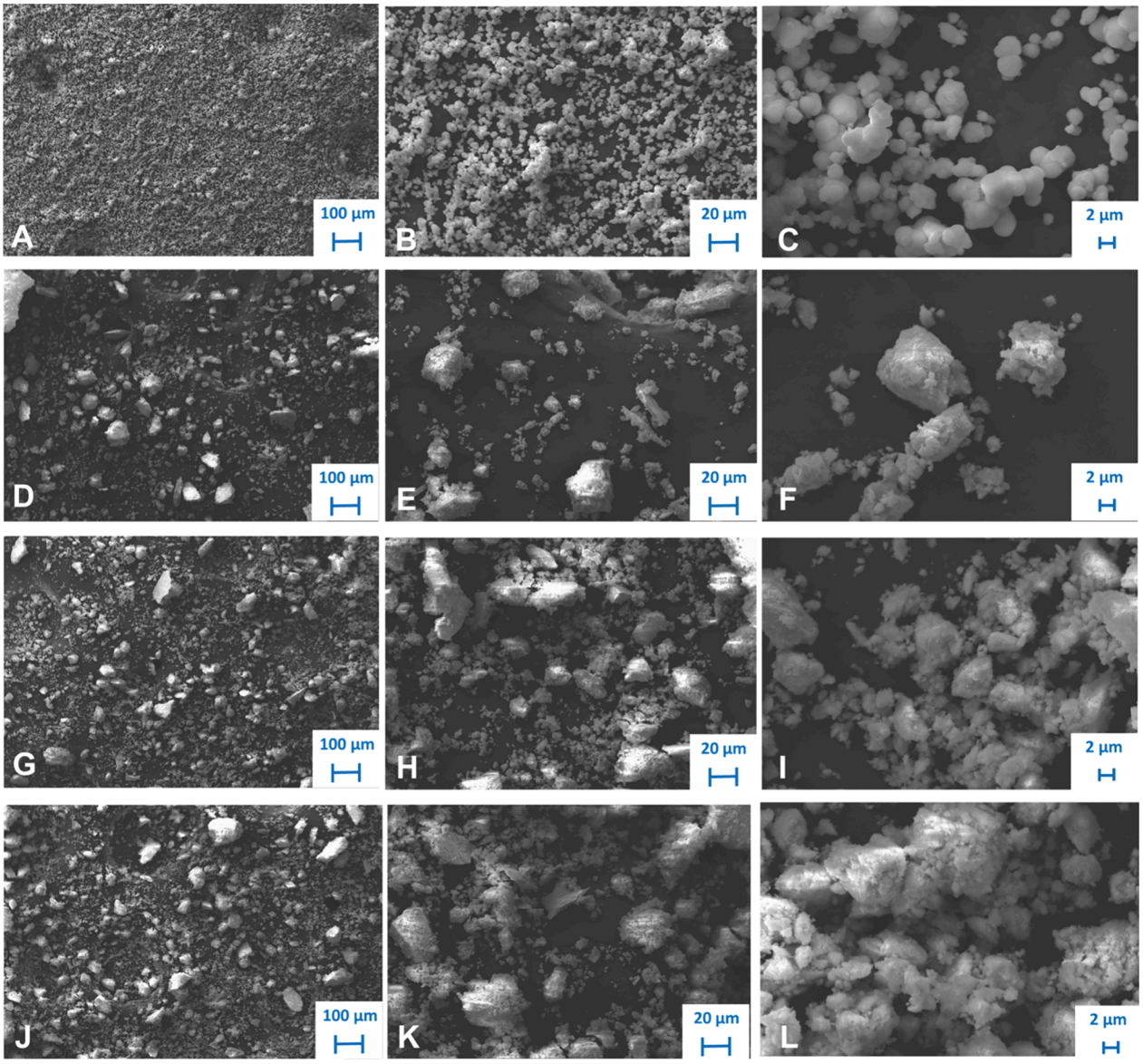

Figure 5. SEM images of (A-C) CeO_2-ESA sample, (D−F) CeO_2−HSA-HE-8h, (G−I) CeO_2-MSA-HE-8h, and (J−L) CeO_2-LSA-HE-8h, at increasing magnification factors.

Raman spectroscopy is a handy tool to follow the presence of Ce^{3+} entities or oxygen vacancies (O_v) in the ceria structure and surface, resulting in the following specific bands: the second-order transversal acoustic (2TA) band at around 260 cm^{-1}, the main F_{2g} band at around 460 cm^{-1}, the defect-induced (D) band at 560−590 cm^{-1}, and the second-order longitudinal optical (2LO) band at 1179 cm^{-1}.[66−68] Figure 6 reports full Raman spectra of the fresh CeO_2 powders and their evolution with increasing milling energy and time. A magnification inset between 420 and 500 cm^{-1} is also reported for every sample to better appreciate the evolution of the F_{2g} band, which is usually associated with the breathing vibration of the O atom between two Ce^{4+} cations in the fluorite lattice. Interestingly, every milled CeO_2 sample exhibits a clear band shift with respect to its fresh counterpart: the F_{2g} shift to lower frequencies is related to the lattice expansion due to the increase in the Ce−O bond length, which is in turn promoted by the formation of Ce^{3+} and oxygen vacancies[66] and the related induced strain.[69] The higher amount of lattice and surface defects can also be deduced by the intensification of the D band at 590 cm^{-1}, which is usually associated with the presence of O_v and Ce^{3+} sites[66,68] and whose growth can be distinctly observed on the MSA and LSA samples, both milled under ME and, most significantly, under HE conditions. Clearly, both intensity and milling time contribute to boosting the number of defects in CeO_2 samples.[58] This is in agreement with the X-ray diffraction evidence, where large strain values were observed after milling, especially for MSA and LSA samples (Table S2).

Remarkably, on HSA samples, no variations in the D band intensity can be observed. However, the signal at 260 cm^{-1} and the variation in the F_{2g} shoulder at ∼400 cm^{-1} can give additional information regarding the morphological modification of samples, since these two bands are linked to surface terminations of CeO_2 crystals. In literature, 2TA bands at 256 and 409 cm^{-1}, the latter usually resulting in a F_{2g} shoulder, are associated with the longitudinal stretching of the topmost O−Ce layers and to the transversal mode of the outermost oxygen

https://doi.org/10.1021/acsomega.3c09926
ACS Omega 2024, 9, 12046−12059

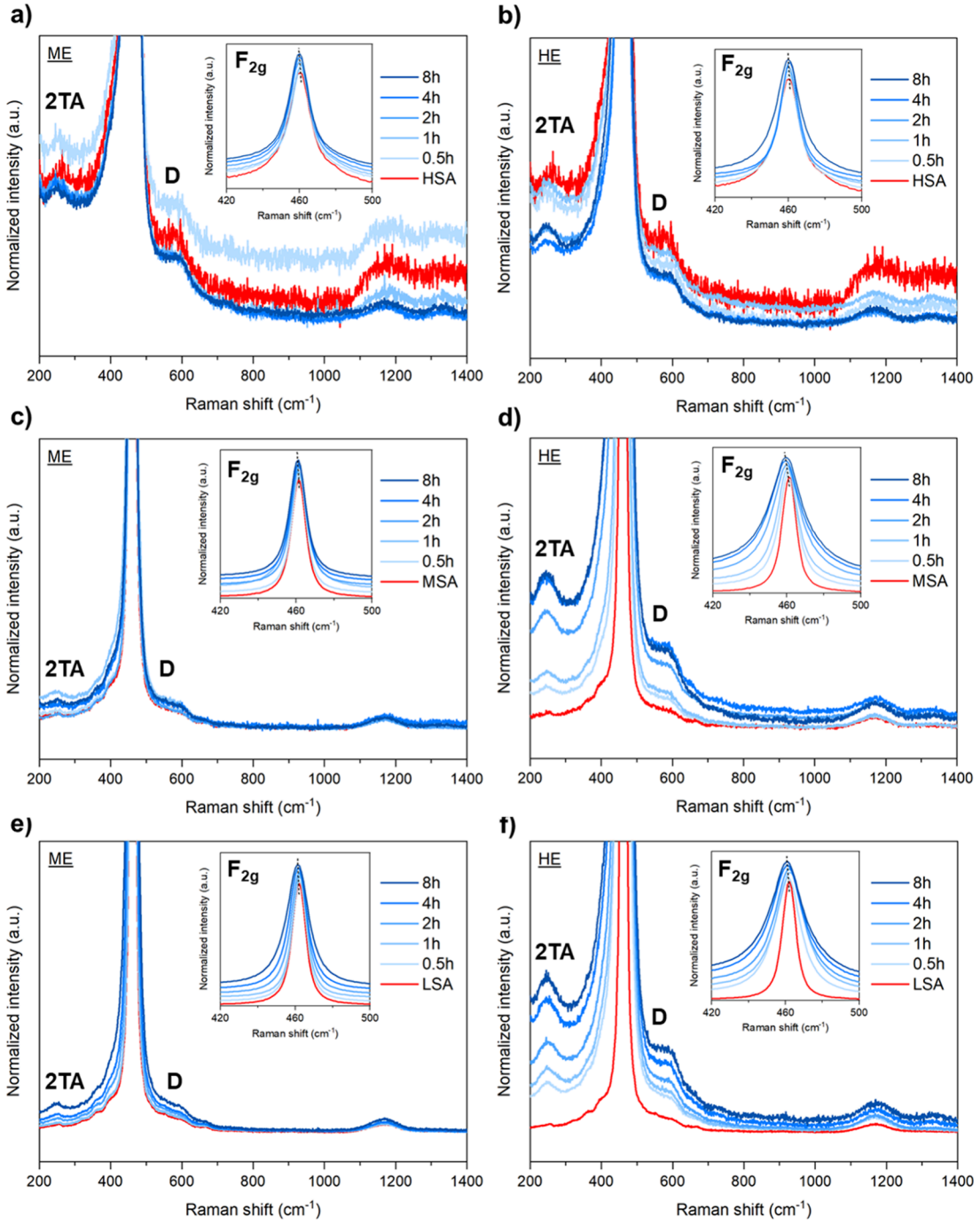

Figure 6. Full Raman spectra collected on (a, b) HSA, (c, d) MSA, and (e, f) LSA samples milled at medium (ME) and high (HE) energy conditions and increasing milling times.

atoms, respectively.[69] A strong increase in the Raman intensity of these bands is then expected for smaller ceria nanoparticles, where more surface terminations are present. Indeed, a huge growth in the 256 cm^{-1} band can be observed for both MSA and LSA samples during HE milling, in which the average crystallite size is immediately reduced. Similar considerations can be made for the ESA sample (Figure S8), where the particle comminution is accompanied by the appearance of surface defects. Conversely, for HSA samples, under HE milling conditions, the 2TA intensity decreased, in accordance with the observed enlargement in crystallite dimension, while no changes in Raman spectra could be detected under ME conditions. The consistency of the Raman shift on the HSA samples is congruent with the preservation of the average crystalline size during the entire milling process under ME conditions (Figure 3), and it further suggests that the highly defective initial surface of HSA ceria is only slightly improved by the milling process. In summary, Raman spectroscopy corroborates the morphological modifications highlighted by XRD analysis and further expands it to reveal surface CeO_2 defectivity variations, which are more significant on the ceria particles initially having the highest degree of lattice order (LSA > MSA > ESA > HSA).

https://doi.org/10.1021/acsomega.3c09926
ACS Omega 2024, 9, 12046−12059

The surface of cerium oxide plays a key role in determining its chemical properties in heterogeneous catalysts, as for example its capacity to easily exchange oxygen species between the lattice and the gas phase, resulting in unique catalytic properties,[1,70] or the ability to act as a metal trap for metal-supported catalysts.[71,72] Different crystal planes and/or the presence of defects on the ceria surface can strongly affect these properties, hence resulting in peculiar catalytic performance.[3,4,7,60] By means of H_2-TPR, we complemented Raman findings to evaluate the effect of milling energy and time on the amount of reactive oxygen species on the CeO_2 surface. As the amount of reactive O* species on the ceria surface depends not only on the exposed surface state but also on the total amount of surface available and exposed to the gas phase,[70,73] Figure 7 reports the amount of reacting H_2 in the low-temperature region (below 500 °C) against the BET surface area. The quantitative analysis clearly shows an increasing trend of H_2 uptake with higher surface area, which is linear for calcined samples (red symbols); for milled samples, the materials subjected to mild energy milling or short time display a similar behavior as their fresh counterpart, while a substantial increase in H_2 consumption is observed on the samples milled at high energy for 8h (HE-8h). Full reducibility profiles are reported in Figure S9 for all samples. These observations suggest that the higher number of defects on the surface generated by milling promotes reducibility of the samples at low temperature, which could be of interest for catalytic and metal-doping application of ceria. The enhanced low-temperature reducibility might be promoted by the Zr doping over the ceria surface,[16] where the introduction of Zr atoms by shear stresses from the milling media might concur in stabilizing the surface defects on the ceria surface.

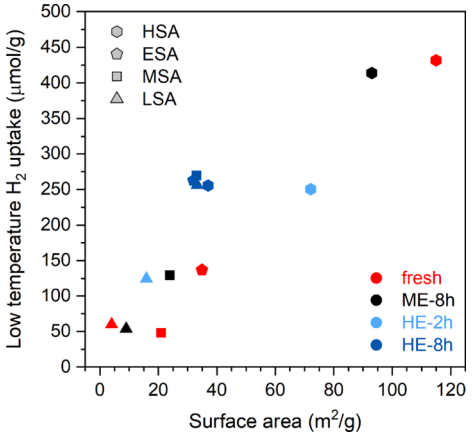

Figure 7. Quantitative H_2 uptake below 500 °C per gram of catalysts as a function of the surface area for selected samples. Red symbols: fresh catalysts; black symbols: milled at mild energy for 8 h; light-blue symbols: milled at high energy for 2 h; dark-blue symbols: milled at high energy for 8 h.

To further investigate the redox behavior of the ceria powders, CO oxidation was used as an efficient test reaction to probe the presence and different nature of labile oxygen species on the milled catalysts under an oxidizing atmosphere.[4,70,73] The full conversion profiles recorded during oxidation tests and calculated rates are reported in Figure S10, while the reactivity in terms of reaction rate at 250 °C is compared in Figure 8 for the most representative samples, i.e., all fresh samples and their counterparts milled at mild and high energy

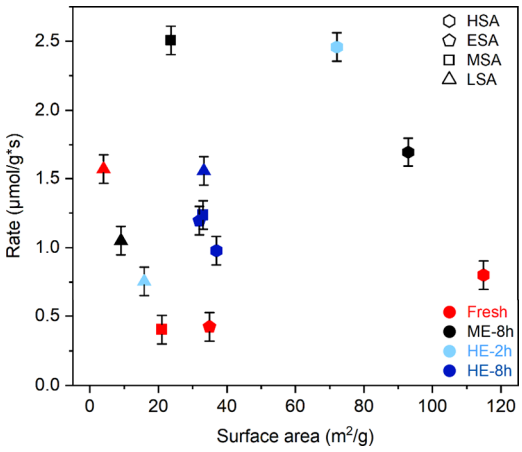

Figure 8. Calculated CO oxidation rates at 250 °C per gram of catalysts as a function of the surface area for selected samples. Red symbols: fresh catalysts; black symbols: milled at mild energy for 8 h; light-blue symbols: milled at high energy for 2 h; blue symbols: milled at high energy for 8 h.

for 8 h, as well as samples milled at high energy for 2 h. To account for the surface area available on the powder catalysts, the reaction rates are plotted against the measured BET surface area, showing a different behavior compared with the measured reducibility under pure H_2 feed (Figure 7). In fact, from the reaction rates in Figure 8 there appears to be no clear trend among catalysts, as expected by the multiple factors affecting reactivity toward CO on CeO_2-based materials.[73] All calcined samples, with the exception of the LSA catalyst, display similar reaction rate values regardless of their surface area. After milling, their activity is significantly increased, especially at milder conditions (mild milling for 8 h, or high energy milling for 2 h), while prolonged high energy milling (HE-8h) appears to be less effective, despite still outperforming the fresh counterpart. The sample calcined at the highest temperature (1200 °C) displays the opposite behavior, where its catalytic performance is initially negatively affected by milling and, at longer milling time under high energy conditions, recovers the catalytic performance. These trends suggest that, as observed in Morphological Features, the initial properties of the calcined powders play a key role in determining the positive or negative effect of milling: in this specific context, CeO_2 with medium-small particles and low CO oxidation activity is enhanced by mechanically induced defects while CeO_2 with large particles calcined at high temperature is already among the best-performing materials for CO oxidation; hence, further changes induced by milling result in a decrease in catalytic performance. Moreover, the lack of correlation between the behavior exhibited by the CeO_2 powders under reducing and oxidizing conditions suggests that the nature of defective sites and related mobile oxygen species are different on the fresh and milled samples,[74] and they are strongly affected by the type of reducing agent (e.g., H_2 vs CO) and by the presence of additional O_2 in the gas feed. Indeed, TPR tests carried out with CO as the reducing agent show a different behavior compared to H_2-TPR experiments, as illustrated in Figure S11, where the calcined LSA sample displays overall a similar uptake of CO compared to the milled catalyst below 500 °C (571 vs 743 μmol/g, respectively) and a much stronger affinity to CO in the full temperature range (up to 900 °C).

https://doi.org/10.1021/acsomega.3c09926
ACS Omega 2024, 9, 12046−12059

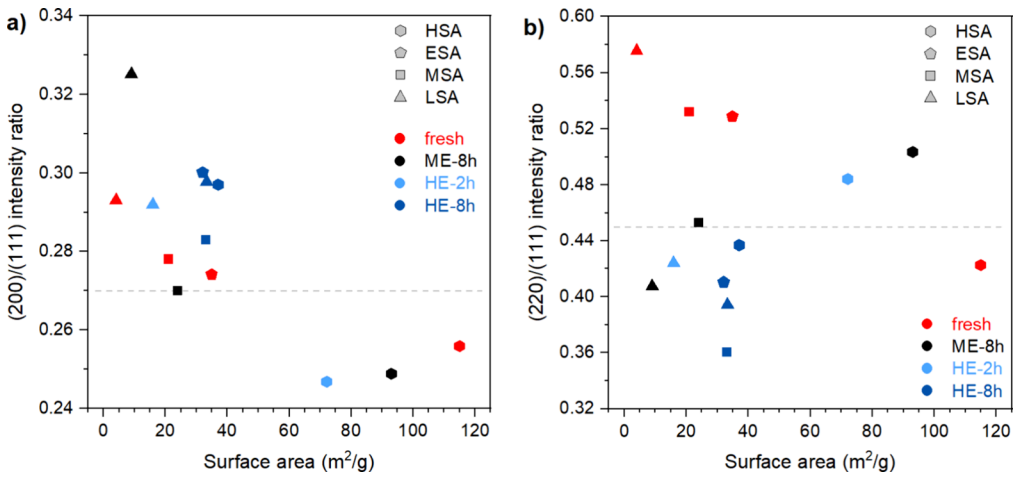

Figure 9. Evolution of the low index reflections (a) (200)/(111) and (b) (220)/(111) ratios on selected samples as a function of the BET surface area. The gray dashed line represents the theoretical value.

Possibly, one important parameter affecting CO oxidation is represented by the exposed CeO_2 surfaces,[60,70] where undercoordinated terminations are characterized by lower oxygen vacancy (O_v) formation and higher CO oxidation activity.[3] The relative growth of the more reactive ceria planes is dependent on the calcination temperature,[3,73] and usually a trade-off between undercoordinated surfaces and total CeO_2 nanoparticle surface area can be achieved to reach optimal catalytic activity.[70,73] In mechanochemistry, the exposed ceria planes are likely also affected by the extra surface energy generated through the stresses during the milling process. This phenomenon helps to explain the odd behavior of the LSA sample and might contribute to the definition of the different activity exhibited by the milled samples compared to their calcined counterpart. XRD and Raman analyses previously showed that crystallite size and strain are strongly affected by the mechanical stresses (Figures 3 and 6 and Table S2); thus, it is likely that the exposed surfaces are also modified. By analyzing qualitatively the intensity ratio of the low index (200) and (220) planes with respect to the main (111) reflection of the CeO_2 cubic lattice, reported in Figure 9 for selected representative samples, it can be observed that, in general, milling promotes the growth of the (200) facet and reduces the frequency of the (220) plane compared to the theoretical values calculated over the model ceria fluorite lattice.[4] An exception is represented by the HSA powders, where the low calcination temperature leads to a disordered state in the fresh sample and milling results in an increase of crystalline order, partially explaining the worse performance under CO oxidation conditions.[73]

Another important factor is represented by the inclusion of zirconia in the outermost ceria surface, as formerly mentioned. In fact, Zr segregation within grain structures or at the grain boundaries might affect oxygen vacancy formation and oxygen mobility in a positive or negative way, respectively, thus affecting CO reactivity.[16] Also, zirconia doping into ceria leads to stabilization of defect sites and higher oxygen storage capacity.[1] Possibly, given that the Zr contamination from the milling media reasonably increases with increasing milling intensity and time, the enhanced surface reducibility observed in H_2-TPR experiments (Figure 7) might be promoted by zirconia inclusion, despite the small amount detected by ICP-MS and LEIS analysis (Tables 3 and Figure S4). Conversely, the CO reactivity appears to be more dependent on the exposure of unstable ceria surfaces, occurring already at low milling intensity and then partially negatively affected by the presence of zirconia on the ceria surface, as shown by high-energy-milled samples.

Table 3. Milling Parameters Used for the Preparation of CeO_2 Powders[a]

energy	short name	frequency (Hz)	number of spheres (N)	diameter of spheres (mm)	total weight of spheres (g)	ball-to-powder ratio (BPR)
mild	ME	15	1	15	10	20
high	HE	50	3	10	10	20

[a]Milling times (τ): 0.5, 1, 2, 4, and 8 h.

CONCLUSIONS

The mechanical stresses released during dry milling synthesis processes influence both the morphology and chemistry of CeO_2 powders, positively or negatively depending on the milling conditions and the properties of the starting material. This study was able to show the main trends affecting CeO_2 powders, rationalizing the effect of milling on the redox and textural properties of the ceria catalysts. Overall, high-energy milling results in the most significant modifications of the pristine CeO_2 structure, even after short milling times, increasing the surface area, reducing the crystallite size, and simultaneously promoting particle aggregation. Conversely, mild milling enables smaller variations of the initial CeO_2 structure and a lower number of induced defects, apparently, which are, however, confined on the surface and still affect particle agglomeration and redox properties. However, the effect of mild vs high milling energy depends also on the starting material properties, as for example the CeO_2 powders calcined at the lowest temperature (550 °C), i.e., with the smallest initial crystallite size, are more sensitive to low energies compared to larger CeO_2 particles.

Particularly interesting is the effect of mechanical stresses on the redox properties of CeO_2: the high number of defects created on the CeO_2 surface results in the creation of a large number of labile O atoms, improving reducibility both quantitatively and in terms of the onset redox temperature. These defects might be further stabilized by the inclusion of Zr

https://doi.org/10.1021/acsomega.3c09926
ACS Omega 2024, 9, 12046−12059

atoms from the milling media to the ceria surface and subsurface lattice, despite being found only in a negligible amount (below 0.6 wt %). Additionally, secondary low index surfaces are promoted over the milled cerium oxide, affecting the reactivity of these defective sites generated by milling with respect to CO. The findings of the present work can be used to rationalize the operational ball-milling parameters of a dry milling process for the preparation of CeO_2 nanopowders and their tuning, depending on the desired final properties.

MATERIALS AND METHODS

Preparation of CeO_2 Powders. Commercial cerium oxide (99.99%) was provided by Rhodia. Before milling, CeO_2 powders were calcined in static air in a Nabertherm muffle oven at 550, 900, 950, or 1200 °C for 4 h (heating rate: 10 °C/min) using a sintered alumina crucible. The calcined powders were then milled in a Fritsch Pulverisette P23 mini-mill at mild and high energy conditions, using a 15 mL ZrO_2 jar, varying in milling time (t), frequency (Hz), number (N), and diameter (ϕ) of grinding balls. A ball-to-powder weight ratio (BPR) equal to 20 was fixed, loading 0.5 g of powders and a total of 10 g of milling spheres. To achieve significantly different milling intensities, which are proportional to ball number and frequency,[52] ME conditions were obtained by loading one 15 mm ZrO_2 sphere in the jar and milling at 15 Hz, while HE conditions were achieved by loading three spheres of 10 mm of diameter and milling at 50 Hz. The calcination temperatures, milling parameters, and times were chosen based on previous studies to ensure respectively a wide range of initial surface area values, diverse milling energy, and increasing time intervals to follow the solid-state transformations of the ceria powders.[40,75] A summary of the operational parameters is given in Table 3.

Characterization. Surface area and pore size analyses were carried out by evaluating N_2 adsorption isotherms at 77 K using a Micromeritics TriStar porosimeter. Surface area and pore size distributions were obtained from adsorption and desorption data following the Brunauer–Emmett–Teller theory (BET) and Barrett–Joyner–Halenda method (BJH), respectively. Before analysis, powder samples (250 mg) were degassed below 100 mTorr at 150 °C for 1.5 h. Powder X-ray diffraction patterns were collected using a Philips X'Pert diffractometer with an X'Celerator detector using Ni-filtered Cu Kα radiation (λ = 1.542 Å) operating at 40 kV and 40 mA, collecting data in the 20–80° 2θ range (0.02° step size, 40 s counting time per step). Scherrer's formula[76] was used to estimate the average ceria crystallite size using the main CeO_2 (111) peak at 28°:

$$d_p = \frac{0.9\lambda}{B \cos \theta}$$

where λ is the X-ray wavelength, 0.9 is a correction value for spherical particles, and B corresponds to the FWHM of the peak corrected by the instrumental error.

$$B = \sqrt{B_{obs}^2 - B_{inst}^2}$$

Rietveld refinement was also carried out using GSAS-II software to obtain the crystallite size, microstrain, and cell parameters of the CeO_2 lattice.[77] Williamson–Hall plots were also used to obtain comparative crystallite size values. Particle size distribution (PSD) was determined by a Horiba LA950 laser scattering particle size analyzer: analyses were performed in water after sonication for 1 min. PSD curves are represented with a logarithmic abscissa. Raman spectra were collected ex situ using an XploRA Plus Micro-Raman system (Horiba, Kyoto, Japan). The CeO_2 samples were excited with the 532 nm radiation (100 mW, 10% filter) at room temperature, and the spectra were acquired with a 50× LWD objective with a resolution of 1 cm^{-1} and 10 accumulations of 15 s. The powder particle morphology was examined by a Zeiss EVO40 scanning electron microscope (SEM); before analysis, the powder samples were placed on a conductive substrate and sputtered with gold. ICP-MS analysis was performed by Mikroanalytisches Labor Pascher (Remagen, Germany) to measure the Zr content of samples. Low-energy ion scattering (LEIS) measurements were performed at IONTOF GmbH in Münster, Germany, using a Qtac 100. The instrument is equipped with a double toroidal analyzer optimized for high mass resolution and high sensitivity simultaneously. The primary ion beam, consisting of ^4He or ^{20}Ne ions at an energy of 3 or 5 keV, respectively, impinges on the sample orthogonally, and scattered ions are collected at a scattering angle of 145°. For each spectrum, the ion beam is scanned across an analysis area of 2 × 2 mm^2, and a total fluence of 1E14 and 1E13 ions/cm^2 was used for 3 keV ^4He and 5 keV ^{20}Ne ions, respectively. At this fluence level, the analysis takes place within the static limit, such that the sample surface is not significantly altered by ion beam damage over the course of the analysis. Prior to the introduction into the vacuum system of the instrument, the sample material was compacted into pellets with a pressure of approximately 5 MPa. Before the analysis, each sample was cleaned in-vacuum by exposure to atomic oxygen extracted from a remote plasma source to fully oxidize the surface and remove adventitious carbon species. The sample cleaning was performed in a UHV preparation chamber directly adjacent to the analysis chamber, at a base pressure level of <1 × 10^{-8} mbar. The microwave plasma source, situated approximately 30 mm above the sample surface, was operated at a microwave power of 5 W and a flow rate of approximately 0.5 mL min^{-1} O_2. This led to a pressure of 3 × 10^{-5} mbar in the preparation chamber during the cleaning process, which took 10 min per sample. The downstream products of the plasma source include oxygen radicals, which remove undesired adsorbed organic species from the sample surface by oxidation. After shutting down the oxygen plasma source, the samples were immediately transferred to the UHV analysis chamber with a base pressure of <5 × 10^{-10} mbar.

TPR experiments were carried out in a Micromeritics AutoChem II 2920 analyzer on 50 mg of catalyst loaded in a U-shaped quartz microreactor. Prior to the reduction step, the sample was heated under N_2 to 350 °C to remove adsorbed contaminants; the sample was held at isothermal conditions for 1 h and then cooled to 50 °C. The gas feed was then switched to 35 mL/min of reducing mixture (4.5% H_2 in N_2), and the temperature was ramped to 900 °C at a heating rate of 10 °C/min. H_2 consumption was monitored with a TCD detector. Quantification of hydrogen consumed was carried out by calibrating the apparatus with reduction of a known amount of CuO to metallic Cu. CO-TPR tests were performed following the same procedure as H_2-TPR, using 50 mL/min of a 5% CO in He gas mixture.

Catalytic Performance. CO oxidation tests were performed in a lab-scale flow reactor setup on 30 mg of sample loaded on a quartz wool bed inside a tubular quartz microreactor (ID = 6 mm). Brooks mass flow controllers were

https://doi.org/10.1021/acsomega.3c09926
ACS Omega 2024, 9, 12046−12059

used to feed a 2% CO, 5% O_2, balanced He, gas mixture (52 mL/min, GHSV ≈ 80,000 h^{-1}), dosing separately 20.8 mL of a 5% CO/He mixture along with 2.6 mL of pure O_2 and 28.6 mL of pure He. The microreactor was inserted in a vertical tube furnace and heated from room temperature to 500 °C at a linear rate of 10 °C/min. Reactants (CO, O_2) and products (CO_2) were continuously monitored with an on line ABB Uras 14 infrared gas analyzer coupled with an ABB Magnos 106 paramagnetic analyzer, and the temperature was measured with a K-type thermocouple placed at the top of the catalytic bed. Prior to the analysis, the analyzer was calibrated using a high-precision 1% CO, 1% CO_2, 1% CH_4 in He gas mixture. The CO oxidation rate was used to compare the catalytic performance of the evaluated materials, calculated as

$$r = \frac{X_{CO} \times F_{CO}}{w_{cat}} [\mathrm{mol_{CO} g^{-1} s^{-1}}]$$

where F_{CO} is the reactant flow (in moles of carbon monoxide per second), w_{cat} is the weight of catalyst loaded in the reactor, and X_{CO} represents the CO conversion:

$$X_{CO}(\%) = \frac{[CO]_{in} - [CO]_T}{[CO]_{in}} \times 100$$

Conversion values were measured continuously during reaction, and the conversion at 250 °C was used for the rate calculation in order to ensure the kinetic regime, i.e., conversion values below 10%.

■ ASSOCIATED CONTENT

Supporting Information

The Supporting Information is available free of charge at https://pubs.acs.org/doi/10.1021/acsomega.3c09926.

BET surface area of all samples (Table S1) and of the ESA sample milled at HE (Figure S1); total pore volume of all samples (Figure S2); pore size distribution measured on the ESA sample at increasing milling times (Figure S3); X-ray diffraction patterns of all samples (Figures S4 and S5); ceria lattice parameter, isostatic strain, and average crystallite size obtained by Rietveld refinement (Table S2); estimated particle size by Scherrer's equation, Rietveld refinement, and Williamson−Hall plot (Table S3); Zr surface coverage measured by LEIS (Table S4); cumulative particle size distribution curves (Figure S6); evolution of the d_{80} on all samples as a function of milling time and energy (Figure S7); Raman spectra of the ESA sample at increasing milling times (Figure S8); full H_2-TPR profiles of selected samples (Figure S9); full CO oxidation light-off curves and reaction rates (Figure S10); CO uptake under CO-TPR tests for CeO_2 LSA and LSA-HE-8h samples (Figure S11) (PDF)

■ AUTHOR INFORMATION

Corresponding Authors

Maila Danielis − *Dipartimento Politecnico e INSTM, Università degli Studi di Udine, Udine 33100, Italy;* orcid.org/0000-0001-8469-9282; Email: maila.danielis@uniud.it

Alessandro Trovarelli − *Dipartimento Politecnico e INSTM, Università degli Studi di Udine, Udine 33100, Italy;* orcid.org/0000-0002-1396-4031; Phone: +39 0432 558855; Email: trovarelli@uniud.it

Authors

Andrea Felli − *Dipartimento Politecnico e INSTM, Università degli Studi di Udine, Udine 33100, Italy;* orcid.org/0000-0003-2474-0305

Matteo Zampol − *Dipartimento Politecnico e INSTM, Università degli Studi di Udine, Udine 33100, Italy*

Nicolas Fonda − *Dipartimento Politecnico e INSTM, Università degli Studi di Udine, Udine 33100, Italy*

Philipp Brüner − *IONTOF GmbH, Münster 48149, Germany*

Thomas Grehl − *IONTOF GmbH, Münster 48149, Germany*

Erika Furlani − *Dipartimento Politecnico e INSTM, Università degli Studi di Udine, Udine 33100, Italy*

Stefano Maschio − *Dipartimento Politecnico e INSTM, Università degli Studi di Udine, Udine 33100, Italy*

Sara Colussi − *Dipartimento Politecnico e INSTM, Università degli Studi di Udine, Udine 33100, Italy;* orcid.org/0000-0001-5316-1746

Complete contact information is available at: https://pubs.acs.org/10.1021/acsomega.3c09926

Author Contributions

M.D. and A.F. carried out the experiments, wrote the manuscript, and conceived the project. M.Z. carried out the experiments. N.F. helped in data acquisition and visualization. P.B., T.G., E.F., and S.M. helped in data acquisition. S.C. and A.T. oversaw the entirety of the project, funding, conceptualization, and manuscript preparation. All authors have contributed and given approval to the final version of the manuscript.

Notes

The authors declare no competing financial interest.

■ ACKNOWLEDGMENTS

Dr. Alfredo Rondinella is kindly acknowledged for SEM images. M.D. and A.F. are grateful for funding under the REACT EU Italian PON 2014-2020 Program, Action IV.4 − Innovation and Action IV.5 − Green (DM 1062, 10/08/2021). M.D. and S.C. also acknowledge the Fondazione CRUI for funding under the "Go for IT" Program (CUP G29C20000830001). A.T. acknowledges the Interconnected Nord-Est Innovation Ecosystem (iNEST) and received funding from the European Union Next-GenerationEU (Piano Nazionale di Ripresa e Resilienza (PNRR) − Missione 4 Componente 2, Investimento 1.5 − D.D. 1058 23/06/2022, ECS00000043, CUP G23C22001130006). This manuscript reflects only the authors' views and opinions; neither the European Union nor the European Commission can be considered responsible for them.

■ REFERENCES

(1) Trovarelli, A.; Fornasiero, P. *Catalysis By Ceria And Related Materials*, 2nd ed.; Catalytic Science Series; Imperial College Press: London, United Kingdom, 2013.

(2) Boaro, M.; Colussi, S.; Trovarelli, A. Ceria-Based Materials in Hydrogenation and Reforming Reactions for CO_2 Valorization. *Front. Chem.* **2019**, 7, 28.

(3) Trovarelli, A.; Llorca, J. Ceria Catalysts at Nanoscale: How Do Crystal Shapes Shape Catalysis? *ACS Catal.* **2017**, 7 (7), 4716−4735.

(4) Aneggi, E.; Wiater, D.; de Leitenburg, C.; Llorca, J.; Trovarelli, A. Shape-Dependent Activity of Ceria in Soot Combustion. *ACS Catal.* **2014**, *4* (1), 172−181.
(5) Vilé, G.; Colussi, S.; Krumeich, F.; Trovarelli, A.; Pérez-Ramírez, J. Opposite Face Sensitivity of CeO_2 in Hydrogenation and Oxidation Catalysis. *Angew. Chem., Int. Ed.* **2014**, *53* (45), 12069−12072.
(6) Agarwal, S.; Zhu, X.; Hensen, E. J. M.; Lefferts, L.; Mojet, B. L. Defect Chemistry of Ceria Nanorods. *J. Phys. Chem. C* **2014**, *118* (8), 4131−4142.
(7) Liu, X.; Zhou, K.; Wang, L.; Wang, B.; Li, Y. Oxygen Vacancy Clusters Promoting Reducibility and Activity of Ceria Nanorods. *J. Am. Chem. Soc.* **2009**, *131* (9), 3140−3141.
(8) Courtois, X.; Bion, N.; Marécot, P.; Duprez, D. Chapter 8 The Role of Cerium-Based Oxides Used as Oxygen Storage Materials in DeNOx Catalysis. In *Stud. Surf. Sci. Catal.*; Granger, P., Pârvulescu, V. I., Eds.; Elsevier, 2007; Vol. *171*, pp 235−259. .
(9) Mai, H.-X.; Sun, L.-D.; Zhang, Y.-W.; Si, R.; Feng, W.; Zhang, H.-P.; Liu, H.-C.; Yan, C.-H. Shape-Selective Synthesis and Oxygen Storage Behavior of Ceria Nanopolyhedra, Nanorods, and Nanocubes. *J. Phys. Chem. B* **2005**, *109* (51), 24380−24385.
(10) Ohtake, N.; Katoh, M.; Sugiyama, S. High Thermal-Stability Ceria Synthesized via Thermal-Hydrolysis Route and Methane-Combustion Performance. *J. Ceram. Soc. JAPAN* **2017**, *125* (2), 57−61.
(11) Ohtake, N.; Yamane, Y.; Nakagawa, K.; Katoh, M.; Sugiyama, S. Hydrothermally Synthesized Ceria with a High Specific Surface Area for Catalytic Conversion of Ethanol to Ethylene. *J. Chem. Eng. Jpn.* **2016**, *49* (2), 197−203.
(12) Tok, A. I. Y.; Boey, F. Y. C.; Dong, Z.; Sun, X. L. Hydrothermal Synthesis of CeO_2 Nano-Particles. *J. Mater. Process. Technol.* **2007**, *190* (1−3), 217−222.
(13) Dong, C.; Zhou, Y.; Ta, N.; Liu, W.; Li, M.; Shen, W. Shape Impact of Nanostructured Ceria on the Dispersion of Pd Species. *Chin. J. Catal.* **2021**, *42* (12), 2234−2241.
(14) Cargnello, M.; Doan-Nguyen, V. V. T.; Gordon, T. R.; Diaz, R. E.; Stach, E. A.; Gorte, R. J.; Fornasiero, P.; Murray, C. B. Control of Metal Nanocrystal Size Reveals Metal-Support Interface Role for Ceria Catalysts. *Science* **2013**, *341* (6147), 771−773.
(15) Farmer, J. A.; Campbell, C. T. Ceria Maintains Smaller Metal Catalyst Particles by Strong Metal-Support Bonding. *Science* **2010**, *329* (5994), 933−936.
(16) Symington, A. R.; Molinari, M.; Statham, J.; Wu, J.; Parker, S. C. The Role of Dopant Segregation on the Oxygen Vacancy Distribution and Oxygen Diffusion in CeO_2 Grain Boundaries. *J. Phys. Energy* **2019**, *1* (4), No. 042005.
(17) Yang, Q.; Wang, Y.; Tian, D.; Wu, H.; Ding, Y.; Lu, X.; Chen, Y.; Lin, B. Enhancing Performance and Stability of Symmetrical Solid Oxide Fuel Cells via Quasi-Symmetrical Ceria-Based Buffer Layers. *Ceram. Int.* **2022**, *48* (19), 27509−27515.
(18) Wen, Y.; Abe, H.; Hirata, A.; Hashimoto, A. Correlation between the Charge-Transport Properties and the 3D-Phase Connectivities in Patterned Pt/CeO_2 Nanostructured Composites: Implications for Solid-Oxide Fuel Cells. *ACS Appl. Nano Mater.* **2021**, *4* (12), 13602−13611.
(19) Jaiswal, N.; Tanwar, K.; Suman, R.; Kumar, D.; Upadhyay, S.; Parkash, O. A Brief Review on Ceria Based Solid Electrolytes for Solid Oxide Fuel Cells. *J. Alloys Compd.* **2019**, *781*, 984−1005.
(20) Lucentini, I.; García Colli, G.; Luzi, C.; Serrano, I.; Soler, L.; Divins, N. J.; Martínez, O. M.; Llorca, J. Modelling and Simulation of Catalytic Ammonia Decomposition over Ni-Ru Deposited on 3D-Printed CeO_2. *Chem. Eng. J.* **2022**, *427*, No. 131756.
(21) Zanco, S. E.; Ambrosetti, M.; Groppi, G.; Tronconi, E.; Mazzotti, M. Heat Transfer Intensification with Packed Open-Cell Foams in TSA Processes for CO_2 Capture. *Chem. Eng. J.* **2022**, *430*, No. 131000.
(22) Balzarotti, R.; Ambrosetti, M.; Arnesano, M.; Anglani, A.; Groppi, G.; Tronconi, E. Periodic Open Cellular Structures (POCS) as Enhanced Catalyst Supports: Optimization of the Coating Procedure and Analysis of Mass Transport. *Appl. Catal. B: Env.* **2021**, *283*, No. 119651.
(23) Lucentini, I.; Serrano, I.; Soler, L.; Divins, N. J.; Llorca, J. Ammonia Decomposition over 3D-Printed CeO_2 Structures Loaded with Ni. *Appl. Catal. A: Gen.* **2020**, *591*, No. 117382.
(24) Lanzutti, A.; Sordetti, F.; Montanari, R.; Varone, A.; Marin, E.; Andreatta, F.; Maschio, S.; Furlani, E.; Magnan, M.; Vaglio, E.; Pakhomova, E.; Sortino, M.; Totis, G.; Fedrizzi, L. Effect of Powder Recycling on Inclusion Content and Distribution in AISI 316L Produced by L-PBF Technique. *J. Mater. Res. Technol.* **2023**, *23*, 3638−3650.
(25) Wang, R.; Xi, L.; Ding, K.; Gökce, B.; Barcikowski, S.; Gu, D. Powder Preparation during Ball Milling and Laser Additive Manufacturing of Aluminum Matrix Nanocomposites: Powder Properties, Processability and Mechanical Property. *Adv. Powder Technol.* **2022**, *33* (8), No. 103687.
(26) Chen, D.; Liu, B.; Xu, W.; Zhang, C.; Guo, E.; Lu, J.; Sun, G.; Pan, Y.; Zhang, J.; Lu, X. Effect of Particle Morphology on the flowability of HDH Ti Powders Treated by High Temperature Ball Milling. *Adv. Powder Technol.* **2022**, *33* (11), No. 103803.
(27) Vogt, M. A. H.; Thill, A. S.; Matte, L. P.; Escudero, C.; Bernardi, F. CeO_{2-x} Nanoparticles Heated to 900°C Afford Nanomaterials without Thermally Induced Mismatches: Implications for Catalyst Carriers. *ACS Appl. Nano Mater.* **2023**, *6* (7), 5712−5720.
(28) Du, C.-B.; Law, Z. X.; Huang, R.-Y.; Tsai, D.-H. Aerosol-Phase Synthesis of Bimetallic NiCu Oxide-Decorated CeO_2 Nanoparticle Cluster for Catalytic Methane Combustion. *Adv. Powder Technol.* **2022**, *33* (8), No. 103649.
(29) Fujiwara, K.; Kayano, S.; Nishijima, M.; Kobayashi, K.; Nanba, T.; Tsujimura, T. Porous NiO Prepared by Flame Spray Pyrolysis for 80 Wt% Ni−CeO_2 Catalyst and Its Activity for CO_2 Methanation. *J. Jpn. Petrol. Inst.* **2021**, *64* (5), 261−270.
(30) Hayakawa, E.; Nakamura, H.; Ohsaki, S.; Watano, S. Dry Mixing of Cathode Composite Powder for All-Solid-State Batteries Using a High-Shear Mixer. *Adv. Powder Technol.* **2022**, *33* (8), No. 103705.
(31) Puente-Martínez, D. E.; Díaz-Guillén, J. A.; Montemayor, S. M.; Díaz-Guillén, J. C.; Burciaga-Díaz, O.; Bazaldúa-Medellín, M. E.; Díaz-Guillén, M. R.; Fuentes, A. F. High Ionic Conductivity in CeO_2 SOFC Solid Electrolytes; Effect of Dy Doping on Their Electrical Properties. *Int. J. Hydrogen Energy* **2020**, *45* (27), 14062−14070.
(32) Torknik, F. S.; Keyanpour-Rad, M.; Maghsoudipour, A.; Choi, G. M. Effect of Microstructure Refinement on Performance of Ni/$Ce_{0.8}Gd_{0.2}O_{1.9}$ Anodes for Low Temperature Solid Oxide Fuel Cell. *Ceram. Int.* **2014**, *40* (1, Part B), 1341−1350.
(33) Kotake, N.; Kuboki, M.; Kiya, S.; Kanda, Y. Influence of Dry and Wet Grinding Conditions on Fineness and Shape of Particle Size Distribution of Product in a Ball Mill. *Adv. Powder Technol.* **2011**, *22* (1), 86−92.
(34) Iwasaki, T. Environmentally Friendly Green Synthesis of Fine Particles by Dry Mechanical Processes Toward SDGs: A Review. *KONA* **2022**, *40*, 2023014.
(35) Ardila-Fierro, K. J.; Hernández, J. G. Sustainability Assessment of Mechanochemistry by Using the Twelve Principles of Green Chemistry. *ChemSusChem* **2021**, *14* (10), 2145−2162.
(36) He, X.; Deng, Y.; Zhang, Y.; He, Q.; Xiao, D.; Peng, M.; Zhao, Y.; Zhang, H.; Luo, R.; Gan, T.; Ji, H.; Ma, D. Mechanochemical Kilogram-Scale Synthesis of Noble Metal Single-Atom Catalysts. *Cell Rep.* **2020**, *1* (1), No. 100004.
(37) Santhanam, P. R.; Dreizin, E. L. Predicting Conditions for Scaled-up Manufacturing of Materials Prepared by Ball Milling. *Powder Technol.* **2012**, *221*, 403−411.
(38) Furlani, E.; Aneggi, E.; de Leitenburg, C.; Maschio, S. High Energy Ball Milling of Titania and Titania−Ceria Powder Mixtures. *Powder Technol.* **2014**, *254*, 591−596.
(39) Zhang, Q.; Saito, F. A Review on Mechanochemical Syntheses of Functional Materials. *Adv. Powder Technol.* **2012**, *23* (5), 523−531.

https://doi.org/10.1021/acsomega.3c09926
ACS Omega 2024, 9, 12046−12059

(40) Trovarelli, A.; Zamar, F.; Llorca, J.; Leitenburg, C. de; Dolcetti, G.; Kiss, J. T. Nanophase Fluorite-Structured CeO_2−ZrO_2 Catalysts Prepared by High-Energy Mechanical Milling. *J. Catal.* **1997**, *169* (2), 490−502.
(41) Rinaudo, M. G.; Beltrán, A. M.; Fernández, A.; Cadús, L. E.; Morales, M. R. Pd Supported on Defective TiO_2 Polymorphic Mixtures: Effect of Metal-Support Interactions upon Glycerol Selective Oxidation. *Results Eng.* **2022**, *16*, No. 100737.
(42) Rainer, D. N.; Morris, R. E. New Avenues for Mechanochemistry in Zeolite Science. *Dalton Trans.* **2021**, *50* (26), 8995−9009.
(43) Yang, L.; Pan, Z.; Tian, Z. Mechanochemical Synthesis of Solid Catalysts and Application in Catalytic Reaction. *ChemCatChem* **2024**, No. e202301519.
(44) Danielis, M.; Colussi, S.; de Leitenburg, C.; Soler, L.; Llorca, J.; Trovarelli, A. Outstanding Methane Oxidation Performance of Palladium-Embedded Ceria Catalysts Prepared by a One-Step Dry Ball-Milling Method. *Angew. Chem., Int. Ed.* **2018**, *57* (32), 10212−10216.
(45) Schreyer, H.; Eckert, R.; Immohr, S.; de Bellis, J.; Felderhoff, M.; Schüth, F. Milling Down to Nanometers: A General Process for the Direct Dry Synthesis of Supported Metal Catalysts. *Angew. Chem., Int. Ed.* **2019**, *58* (33), 11262−11265.
(46) Amrute, A. P.; De Bellis, J.; Felderhoff, M.; Schüth, F. Mechanochemical Synthesis of Catalytic Materials. *Chem.—Eur. J.* **2021**, *27* (23), 6819−6847.
(47) Braga, A.; Armengol-Profitós, M.; Pascua-Solé, L.; Vendrell, X.; Soler, L.; Serrano, I.; Villar-Garcia, I. J.; Pérez-Dieste, V.; Divins, N. J.; Llorca, J. Bimetallic NiFe Nanoparticles Supported on CeO_2 as Catalysts for Methane Steam Reforming. *ACS Appl. Nano Mater.* **2023**, *6* (9), 7173−7185.
(48) Jiménez, J. D.; Betancourt, L. E.; Danielis, M.; Zhang, H.; Zhang, F.; Orozco, I.; Xu, W.; Llorca, J.; Liu, P.; Trovarelli, A.; Rodríguez, J. A.; Colussi, S.; Senanayake, S. D. Identification of Highly Selective Surface Pathways for Methane Dry Reforming Using Mechanochemical Synthesis of Pd−CeO_2. *ACS Catal.* **2022**, *12* (20), 12809−12822.
(49) Danielis, M.; Betancourt, L. E.; Orozco, I.; Divins, N. J.; Llorca, J.; Rodríguez, J. A.; Senanayake, S. D.; Colussi, S.; Trovarelli, A. Methane Oxidation Activity and Nanoscale Characterization of Pd/CeO_2 Catalysts Prepared by Dry Milling Pd Acetate and Ceria. *Appl. Catal. B: Env.* **2021**, *282*, No. 119567.
(50) Mussio, A.; Danielis, M.; Divins, N. J.; Llorca, J.; Colussi, S.; Trovarelli, A. Structural Evolution of Bimetallic PtPd/CeO_2 Methane Oxidation Catalysts Prepared by Dry Milling. *ACS Appl. Mater. Interfaces* **2021**, *13* (27), 31614−31623.
(51) Divins, N. J.; Braga, A.; Vendrell, X.; Serrano, I.; Garcia, X.; Soler, L.; Lucentini, I.; Danielis, M.; Mussio, A.; Colussi, S.; Villar-Garcia, I. J.; Escudero, C.; Trovarelli, A.; Llorca, J. Investigation of the Evolution of Pd-Pt Supported on Ceria for Dry and Wet Methane Oxidation. *Nat. Commun.* **2022**, *13* (1), 5080.
(52) Danielis, M.; Colussi, S.; de Leitenburg, C.; Soler, L.; Llorca, J.; Trovarelli, A. The Effect of Milling Parameters on the Mechanochemical Synthesis of Pd−CeO_2 Methane Oxidation Catalysts. *Catal. Sci. Technol.* **2019**, *9* (16), 4232−4238.
(53) Do, J.-L.; Friščić, T. Mechanochemistry: A Force of Synthesis. *ACS Cent. Sci.* **2017**, *3* (1), 13−19.
(54) Danielis, M.; Colussi, S.; Llorca, J.; Dolan, R. H.; Cavataio, G.; Trovarelli, A. Pd/CeO_2 Catalysts Prepared by Solvent-Free Mechanochemical Route for Methane Abatement in Natural Gas Fueled Vehicles. *Ind. Eng. Chem. Res.* **2021**, *60* (18), 6435−6445.
(55) Rinaudo, M. G.; Pecchi, G.; Cadús, L. E.; Morales, M. R. Is Mechanochemical Activation Always an Asset? The Case of Pd/CeO_2 Catalysts for Glycerol Selective Oxidation. *Ceram. Int.* **2023**, *49* (11 part B), 18614−18623.
(56) Šepelák, V.; Bégin-Colin, S.; Le Caër, G. Transformations in Oxides Induced by High-Energy Ball-Milling. *Dalton Trans.* **2012**, *41* (39), 11927.
(57) Rinaudo, M. G.; Cadús, L. E.; Morales, M. R. Mechanochemical Activation of CeO_2 in Order to Boost Physicochemical Properties for Catalytic Applications. *Eng. Proc.* **2023**, *56* (1), 49.
(58) Banerjee, A.; Gupta, R.; Balani, K. Non-Monotonic Lattice Parameter Variation in Ball-Milled Ceria. *J. Mater. Sci.* **2015**, *50* (19), 6349−6358.
(59) Orozco, L. F.; Nguyen, D.-H.; Delenne, J.-Y.; Sornay, P.; Radjai, F. Discrete-Element Simulations of Comminution in Rotating Drums: Effects of Grinding Media. *Powder Technol.* **2020**, *362*, 157−167.
(60) Aneggi, E.; Llorca, J.; Boaro, M.; Trovarelli, A. Surface-Structure Sensitivity of CO Oxidation over Polycrystalline Ceria Powders. *J. Catal.* **2005**, *234* (1), 88−95.
(61) Liotta, L. F.; Macaluso, A.; Longo, A.; Pantaleo, G.; Martorana, A.; Deganello, G. Effects of Redox Treatments on the Structural Composition of a Ceria−Zirconia Oxide for Application in the Three-Way Catalysis. *Appl. Catal. A: Gen.* **2003**, *240* (1), 295−307.
(62) Enayati, M. H.; Mohamed, F. A. Application of Mechanical Alloying/Milling for Synthesis of Nanocrystalline and Amorphous Materials. *Int. Mater. Rev.* **2014**, *59* (7), 394−416.
(63) Schwarz, R. B.; Koch, C. C. Formation of Amorphous Alloys by the Mechanical Alloying of Crystalline Powders of Pure Metals and Powders of Intermetallics. *Appl. Phys. Lett.* **1986**, *49* (3), 146−148.
(64) Wang, M. H.; Yang, R. Y.; Yu, A. B. DEM Investigation of Energy Distribution and Particle Breakage in Tumbling Ball Mills. *Powder Technol.* **2012**, *223*, 83−91.
(65) Buyanov, R. A.; Molchanov, V. V.; Boldyrev, V. V. Mechanochemical Activation as a Tool of Increasing Catalytic Activity. *Catal. Today* **2009**, *144* (3−4), 212−218.
(66) Xu, Y.; Wang, F.; Liu, X.; Liu, Y.; Luo, M.; Teng, B.; Fan, M.; Liu, X. Resolving a Decade-Long Question of Oxygen Defects in Raman Spectra of Ceria-Based Catalysts at Atomic Level. *J. Phys. Chem. C* **2019**, *123* (31), 18889−18894.
(67) Filtschew, A.; Hofmann, K.; Hess, C. Ceria and Its Defect Structure: New Insights from a Combined Spectroscopic Approach. *J. Phys. Chem. C* **2016**, *120* (12), 6694−6703.
(68) Wu, Z.; Li, M.; Howe, J.; Meyer, H. M.; Overbury, S. H. Probing Defect Sites on CeO_2 Nanocrystals with Well-Defined Surface Planes by Raman Spectroscopy and O_2 Adsorption. *Langmuir* **2010**, *26* (21), 16595−16606.
(69) Schilling, C.; Hofmann, A.; Hess, C.; Ganduglia-Pirovano, M. V. Raman Spectra of Polycrystalline CeO_2: A Density Functional Theory Study. *J. Phys. Chem. C* **2017**, *121* (38), 20834−20849.
(70) Sayle, T. X. T.; Parker, S. C.; Sayle, D. C. Oxidising CO to CO_2 Using Ceria Nanoparticles. *Phys. Chem. Chem. Phys.* **2005**, *7* (15), 2936.
(71) Spezzati, G.; Su, Y.; Hofmann, J. P.; Benavidez, A. D.; DeLaRiva, A. T.; McCabe, J.; Datye, A. K.; Hensen, E. J. M. Atomically Dispersed Pd−O Species on CeO_2 (111) as Highly Active Sites for Low-Temperature CO Oxidation. *ACS Catal.* **2017**, *7* (10), 6887−6891.
(72) Jones, J.; Xiong, H.; DeLaRiva, A. T.; Peterson, E. J.; Pham, H.; Challa, S. R.; Qi, G.; Oh, S.; Wiebenga, M. H.; Pereira Hernandez, X. I.; Wang, Y.; Datye, A. K. Thermally Stable Single-Atom Platinum-on-Ceria Catalysts via Atom Trapping. *Science* **2016**, *353* (6295), 150−154.
(73) Lundberg, M.; Skårman, B.; Reine Wallenberg, L. Crystallography and Porosity Effects of CO Conversion on Mesoporous CeO_2. *Microporous Mesoporous Mater.* **2004**, *69* (3), 187−195.
(74) Dean, J. M.; Chun, W.; Jen, H.-W.; Benson, D. A.; McCabe, R. W.; Graham, G. W. Modification of Low-Grade Ceria by High-Energy Mechanical Milling: Changes in Phase Composition, Reducibility, and Oxygen Storage Capacity. *Appl. Catal. A: Gen.* **2001**, *207* (1), 379−386.
(75) Aneggi, E.; Rico-Perez, V.; de Leitenburg, C.; Maschio, S.; Soler, L.; Llorca, J.; Trovarelli, A. Ceria-Zirconia Particles Wrapped in a 2D Carbon Envelope: Improved Low-Temperature Oxygen Transfer and Oxidation Activity. *Angew. Chem., Int. Ed.* **2015**, *54* (47), 14040−14043.

https://doi.org/10.1021/acsomega.3c09926
ACS Omega 2024, 9, 12046−12059

(76) Patterson, A. L. The Scherrer Formula for X-Ray Particle Size Determination. *Phys. Rev.* **1939**, *56* (10), 978−982.
(77) Toby, B. H.; Von Dreele, R. B. GSAS-II: The Genesis of a Modern Open-Source All Purpose Crystallography Software Package. *J. Appl. Crystallogr.* **2013**, *46* (2), 544−549.

https://doi.org/10.1021/acsomega.3c09926
ACS Omega 2024, 9, 12046−12059